SCIEPublish

Article

Preparation, Characterization and Performance Assessment of Metal Complexes of *Curcuma longa* Extract as Sensitizers for Dye-Sensitized Solar Cells

Ekemini Ituen [1,*], Chidozie Ezekwem [2], Babagana Shuaibu [3], Muhaliyu Abdulmojeed [4], Selina Udegbe [5], Rose Usoro [1], Iniubong Okon [1], Udoinyang Inyang [6] and Leo Osuji [7]

[1] Computational Materials Science Group, TETFUND Centre of Excellence in Computational Intelligence, University of Uyo, Uyo 520101, Nigeria; ruusoro@gmail.com (R.U.); okoniniubongg@gmail.com (I.O.)
[2] Department of Mechanical Engineering, University of Port Harcourt, Port Harcourt 500272, Nigeria; chidozie.ezekwem@uniport.edu.ng (C.E.)
[3] School of Water, Energy and Environment (SWEE), Cranfield University, Bedford MK43 0AL, UK; shuaibu.babagana.049@cranfield.ac.uk (B.S.)
[4] Department of Chemistry, Islamic University of Madinah, Madinah 42351, Saudi Arabia; mualiyope@students.unilorin.edu.ng (M.A.)
[5] Energy Commission of Nigeria, Benin 300001, Nigeria; udegbe.s@ncee.org.ng (S.U.)
[6] Department of Data Science, Faculty of Computing, University of Uyo, Uyo 520003, Nigeria; udoinyanginyang@uniuyo.edu.ng (U.I.)
[7] Department of Pure and Industrial Chemistry, University of Port Harcourt, Port Harcourt 500272, Nigeria; leo.osuji@uniport.edu.ng (L.O.)

* Corresponding author. E-mail: ekeminiituen@uniuyo.edu.ng (E.I.)

Received: 22 October 2025; Revised: 5 November 2025; Accepted: 25 November 2025; Available online: 1 December 2025

ABSTRACT: The dye extract of *Curcuma longa* (turmeric), which is very rich in curcumin, was chemically modified by complexation reaction with Zn^{2+}, Cu^{2+}, and Fe^{3+} ions to enhance its stability, electron transfer and photovoltaic performance. The dye and complexes were characterized by Ultraviolet-Visible (UV-Vis) absorption and Fourier Transform Infra-Red (FTIR) spectroscopy of potential chromophores and functional groups. The spectral data obtained indicated that the curcuminoid ligands were successfully coordinated with the metal centers, resulting in red-shifted absorption bands from beyond 460 nm and C=O vibrational frequency decreasing below 1650 cm^{-1}. Complexation reaction resulted in improved photochemical response and enhanced light-harvesting potential. When compared, the solar cells fabricated with titanium dioxide (TiO_2) photoanodes sensitized by the complexes afforded improvement in the magnitude of short-circuit current density as well as power conversion efficiency compared to the devices sensitized with the crude extract. Among the three complexes, the Zn-complex afforded the highest efficiency (1.20%), attributed to favourable electronic coupling and reduced recombination losses. Computational studies conducted through quantum chemical calculations based on the curcumin structure supported the experimental findings. The findings from this study demonstrate that metal ions-natural dye complexes have potential for application as low-cost, eco-friendly and sustainable sensitizers, thereby opening a novel horizon in green photovoltaic technologies.

Keywords: *Curcuma longa*; Dye-sensitized solar cells; FTIR; HOMO-LUMO; Natural dye complexes; Photovoltaics

1. Introduction

The global drive for renewable and sustainable energy sources has intensified the search for efficient third-generation photovoltaic technologies. Among these, dye-sensitized solar cells (DSSCs) have attracted significant attention as promising alternatives to conventional silicon-based solar cells. Their advantages, such as low fabrication cost, ease of assembly, and suitability for flexible and semi-transparent applications, make them appealing for both

https://doi.org/10.70322/gct.2025.10022

research and commercial deployment. In a typical DSSC, the photosensitizer plays a central role by capturing incident light and injecting photoexcited electrons into the conduction band of the semiconductor, usually TiO_2 [1].

Traditionally, ruthenium(II)-based complexes have been common sensitizers, offering impressive power conversion efficiencies and long-term stability [2]. However, due to their high cost, limited availability, and environmental concerns, interest in greener, more sustainable alternatives has grown. Natural dyes derived from plants have emerged as attractive candidates because they are low-cost, biodegradable, and eco-friendly. A variety of plant pigments, such as anthocyanins, betalains, chlorophylls, and flavonoids, have been explored as photosensitizers and have demonstrated moderate efficiencies in DSSCs [3–6].

Despite these advantages, the major challenge that limits the practical deployment of natural dyes in DSSCs is their poor photochemical and thermal stability, as well as their narrow absorption spectra and weak binding to TiO_2 surfaces [7]. These shortcomings often result in rapid degradation under illumination and limited long-term performance, thereby undermining the sustainability advantage they offer. Therefore, improving the stability, electronic characteristics, and anchoring ability of natural dyes remains a crucial challenge in the advancement of bio-derived DSSC technologies.

Curcuma longa (turmeric) is widely known for its culinary and medicinal applications and has recently gained attention as a potential natural sensitizer for DSSCs [8–10]. This is due to its rich content of curcuminoids, particularly curcumin, which exhibits strong visible light absorption [11]. In countries like Nigeria, large quantities of harvested turmeric deteriorate before reaching the market due to inadequate storage infrastructure and post-harvest handling challenges. Repurposing such surplus or spoiled turmeric as a renewable raw material for dye extraction will not only reduce agricultural waste but will also support sustainable energy production and rural economic growth.

Curcumin, the primary chromophore in *Curcuma longa*, is a phenolic compound with a conjugated diketone (enol) structure (Figure 1) that promotes visible light absorption and allows for potential coordination with transition metal ions. However, just as most plant derived dyes, native curcumin dyes suffer from rapid photodegradation and poor thermal stability, limiting their use in practical solar devices. One promising strategy to overcome these challenges is metal complexation, where transition metal ions can be coordinated with curcuminoid ligands to form stable complexes. This coordination may enhance electron delocalization, improve molar absorptivity, and stabilize the enolic form of curcumin against photodecomposition [12–14]. The metal-curcumin complexes are expected to facilitate more efficient electron injection into TiO_2 and improve interfacial charge transfer kinetics within the DSSC system.

Motivated by these considerations, this study was designed to synthesize and characterize selected transition metal complexes of *Curcuma longa* dye extract and evaluate their photovoltaic performance as sensitizers in TiO_2-based DSSCs for the first time. The work seeks to provide new insights into how metal complexation can enhance the stability, light-harvesting efficiency, and charge transfer behaviour of natural dye-based systems. By leveraging an abundant, renewable plant resource and introducing a stability enhancing coordination strategy, this study contributes to the development of greener, more sustainable photovoltaic technologies.

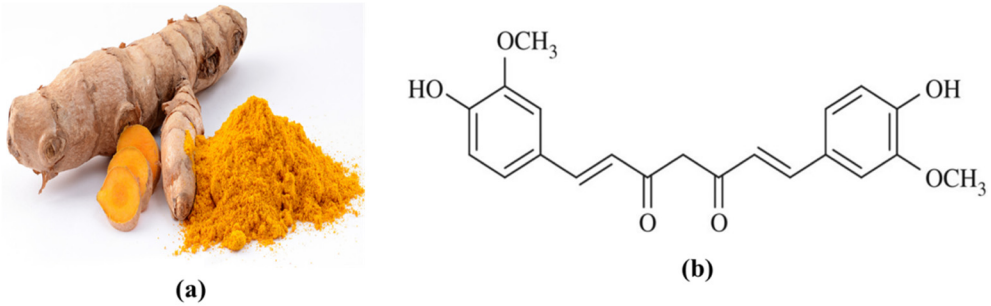

Figure 1. (**a**) Pictures of *Curcuma longa* and (**b**) molecular structure of curcumin.

2. Materials and Methods

2.1. Materials Collection and Pretreatment

Fresh rhizomes of *Curcuma longa* (turmeric) were purchased from commercial suppliers at Akpan Andem market in Uyo, Akwa Ibom state, Nigeria. They were conveyed to our laboratory where they were first washed thoroughly under running tap water to remove the soil, grit and debris. The washed rhizomes were rinsed in several changes of distilled water to ensure that all contaminants were removed. The cleaned rhizomes were peeled to remove the outer skin, then sliced and dried in an oven at 50 °C until reaching constant weight. The dried rhizomes were ground into fine

powder (Figure 1a) using a laboratory grinder, and the powder was stored in air-tight containers, protected from light, prior to extraction. Analytical grade zinc acetate dihydrate, copper acetate monohydrate and ferric chloride hexahydrate were used as metal ion sources. Titanium dioxide nanopowder, platinum-coated counter electrode, fluorine-doped tin oxide (FTO) glass, and iodide electrolyte were used for the dye-sensitised solar cell fabrication.

2.2. Extraction of Curcuma longa Dye

About 100.0 g of turmeric powder was macerated with 1000 mL of absolute ethanol at 40 °C for 6 h. The mixture was filtered, followed by concentration using a rotary evaporator at 40 °C to gradually drive out the solvent. An aliquot of the ethanolic concentrate was diluted with warm deionized water (1:1) to reduce ethanol strength to about 50% *v*/*v* and promote phase separation of non-polars. The mixture was transferred into a separating funnel, and an equivalent volume of n-hexane was added to 10 mL of brine, shaken gently. The n-hexane (upper) layer, which contains fats, oils/essential oils, was collected. This was repeated thrice with fresh n-hexane. The defatted hydroalcoholic extract was stored in amber vials, labelled as *Curcuma longa* extract (CLE) and cooled in a refrigerator.

2.3. Preparation of Metal Complexes

About 100 mg (0.27 mmol) of CLE was used directly as ligand precursor and was dissolved in 25 mL of warm absolute ethanol with gentle continuous stirring until complete dissolution. To facilitate enolate formation, 0.5 mmol of sodium acetate was added, and the pH was adjusted to 8–9 [15]. This ligand solution was used for all the complexation steps. For the zinc complex, 0.135 mmol (29.7 mg) of zinc acetate dihydrate was dissolved in 10 mL of ethanol, and the resulting solution was added dropwise to the ligand solution under stirring at room temperature until a ligand solution to zinc acetate ratio was 2:1 [16]. The mixture was stirred for 1 h during which a red precipitate gradually formed. The solid was collected by filtration, washed with 5 mL methanol, dried in an oven at 40 °C and labelled as *Curcuma longa* extract-zinc complex (Zn-CLE).

For the copper complex (Cu-CLE), 0.135 mmol (27.2 mg) of copper (II) acetate monohydrate was dissolved in 10 mL of ethanol and added to the ligand solution under a nitrogen atmosphere. The mixture was stirred at 50 °C for 2 h when a deep brownish-red colouration was observed. The crude solid was collected after concentration of the extract in a rotary evaporator and subsequently drying in an oven at 40 °C [17].

For the iron complex (Fe-CLE), 0.120 mmol (32.4 mg) of ferric chloride hexahydrate was dissolved in 10 mL of ethanol, and the solution was added slowly to the ligand solution at a 2:1 ligand to metal ratio under a nitrogen atmosphere [18]. The mixture was refluxed at 70 °C for 6 h with continuous stirring. Upon cooling, a dark reddish-brown precipitate was obtained, which was washed with 10 mL of ethanol and dried in an oven at 40 °C.

2.4. Characterization

The extract (CLE) and the metal complexes were characterized by UV-Vis and FTIR spectroscopic techniques. For UV-Vis, the absorption spectra were recorded using a Cary 60 UV-Vis spectrophotometer (Agilent Technologies, Santa Clara, CA, USA) over the wavelength range of 200–800 nm. Samples were prepared in ethanol, and absorbance was measured relative to a blank. The UV-Vis spectra were used to identify characteristic absorption bands associated with the natural extract and to monitor changes upon complexation with metal ions. FTIR analyses were performed using a Shimadzu FTIR-8400s spectrophotometer (Shimadzu Corporation, Kyoto, Japan) in the range of 500–4000 cm^{-1}. Samples were prepared either as KBr pellets, and the obtained spectra were used to identify functional groups in the extract and to confirm coordination between the metal ions and specific functional groups in the complexes.

2.5. Fabrication of DSSCs

FTO glass substrates were cleaned with ethanol and water. A TiO_2 paste was applied onto the conductive side using the doctor-blade method to make a uniform film about 12 μm thick [19]. The films were dried and then sintered at 450 °C for 30 min to improve crystallinity and remove organics. After cooling, the TiO_2 electrodes were soaked in ethanolic solutions of the CLE and the metal–CLE complexes for 24 h in the dark to allow dye adsorption. A platinum-coated FTO glass was used as the counter electrode. The two electrodes were assembled face-to-face with a spacer to create a small gap, which was filled with an iodide/triiodide electrolyte containing 0.5 M iodine (I_2) and 5 M potassium iodide (KI). The active surface area of the electrodes was approximately 0.16 cm^2. After sealing, the assembled DSSC was ready for photovoltaic measurements under simulated sunlight.

2.6. Photovoltaic Measurements

The photovoltaic performance was evaluated under simulated solar illumination using a solar simulator at AM 1.5 G, 100 mW·cm^{-2}, with all measurements taken under ambient conditions. The current density–voltage (J-V) characteristics were recorded using a digital source meter. The photoanode active area was fixed at 0.25 cm^2, and all cells were masked during measurement to minimize edge effects. From the resulting J-V plots, key performance parameters such as open-circuit voltage (V_{oc}), short-circuit current density (J_{sc}), fill factor (FF), and power conversion efficiency (η) were determined as described below [19,20].

The J_{sc} was obtained directly from the current density at zero voltage, while V_{oc} was taken as the voltage when the current density became zero: The FF was computed using the ratio of the maximum output power point to the product of V_{oc} and J_{sc} as shown in Equation (1).

$$\mathrm{FF} = \frac{J_{\max} V_{\max}}{J_{sc} V_{oc}} \tag{1}$$

The magnitude of η was then determined using Equation (2).

$$\eta = 100 \times \frac{J_{sc} V_{oc}}{P_{in}} \times \mathrm{FF} \tag{2}$$

where P_{in} is the incident light power density (100 mW·cm^{-2}). These parameters were used to quantify the ability of the device to convert light into electricity, with J_{sc} representing photocurrent generation, V_{oc} the potential difference, FF the internal losses of the cell, and η the total energy conversion efficiency.

2.7. Determination of Photoelectrochemical Parameters

The parameters of interest determined to assess photon absorption and charge-transfer processes were light-harvesting efficiency (LHE), incident photon-to-current conversion efficiency (PCE), and electron injection rate (EIR). The LHE was derived from absorbance $A_{\lambda_{max}}$ of the dye-coated TiO_2 films at their absorption maxima, measured using UV-Vis spectroscopy, according to Equation (3) [21].

$$\mathrm{LHE} = 1 - 10^{-A_{\lambda_{max}}} \tag{3}$$

The PCE values were measured as a function of wavelength using a solar simulator coupled to a monochromator. The photocurrent density (J_λ) at each wavelength (λ) and the corresponding light intensity P_{in} were used to calculate PCE according to Equation (4) [21].

$$\mathrm{PCE}\ (\%) = 100\left(\frac{1240 J_\lambda}{\lambda P_{in}}\right) \tag{4}$$

The EIR was estimated from the relative ratio between the maximum PCE and LHE values of each dye using Equation (5) [21].

$$\mathrm{EIR} = \frac{\mathrm{PCE}}{\mathrm{LHE}} \tag{5}$$

The resulting PCE spectra were compared with the corresponding absorption spectra to confirm spectral overlap and verify that the measured photocurrents arose predominantly from photoexcitation of the sensitizers.

2.8. Computational Studies

The structure of curcumin was optimized with the use of the Fporcite module in the Materials Studio Accerys software suite, and the procedures reported in earlier literature were followed. The Dmol^3 module was used for quantum chemical calculations, using B3LYP functional in the density functional theory (DFT) domain. Orbital energies of the highest occupied molecular orbital (*HOMO*) and lowest unoccupied molecular orbital (*LUMO*) were computed and results used to determine other quantum descriptors namely, band gap energy (Δ*E*), electronegativity (χ), ionization energy (*IE*), electron affinity (*EA*), global softness (*σ*) and global hardness (*η*) as expressed in Equations (6)–(11) [22].

$$\Delta E = E_{LUMO} - E_{HOMO} \tag{6}$$

$$IE = -E_{HOMO} \quad (7)$$

$$EA = -E_{LUMO} \quad (8)$$

$$\chi = \frac{1}{2}(IE + EA) \quad (9)$$

$$\eta = \frac{1}{2}(IE - EA) \quad (10)$$

$$\sigma = \frac{1}{\eta} \quad (11)$$

3. Results and Discussion

3.1. Extraction Yield and Basic Observations

Out of the 100 g of the turmeric powder that was macerated in ethanol, the concentrated crude extract that remained after solvent removal weighed about 8.7 g, giving a yield of roughly 8.7% *w/w*. This value is in good agreement with the typical curcuminoid yield range of 7–10% reported for turmeric rhizomes [23] and also signifies that the extraction process was efficient. The extract was a dark yellow to brown semi-solid material and exhibited a characteristic turmeric smell. When it was dissolved in ethanol, it gave a deep yellow solution that could show strong visible absorption, which is typical of curcuminoids [24].

The extract remained stable for several days when stored in amber vials at 4 °C. No phase separation or crystallization was observed during storage. When the extract was used as a ligand precursor in metal complexation reactions, clear colour changes were seen. For example, the zinc complex produced a bright reddish-orange precipitate, the copper complex produced a deeper brownish-red material, while the iron complex produced a darker red-brown solid. These visual changes were the first indication that coordination had taken place between the curcuminoid molecules and the metal salts. The solids obtained were more stable in air and light compared to the crude extract solution, which is consistent with reports that complexation stabilizes the enolic structure of curcumin [25].

3.2. UV-Vis Absorption

The CLE showed a strong peak at 425 nm (Figure 2), a band in the blue-violet region, typical of curcuminoids [26]. Complexation with the metal ions caused a shift to longer wavelengths (bathochromic shift) and changed the band shape. The Zn-complex showed a moderate red shift to 455 nm. The spectrum of Cu-complex shifted further and became broader. The Fe-complex shifted the most and gave a broad, lower-intensity band with a long tail into the visible region. These spectral changes usually influence light harvesting characteristics in DSSCs and may likely change the short-circuit current and injection behaviour [27].

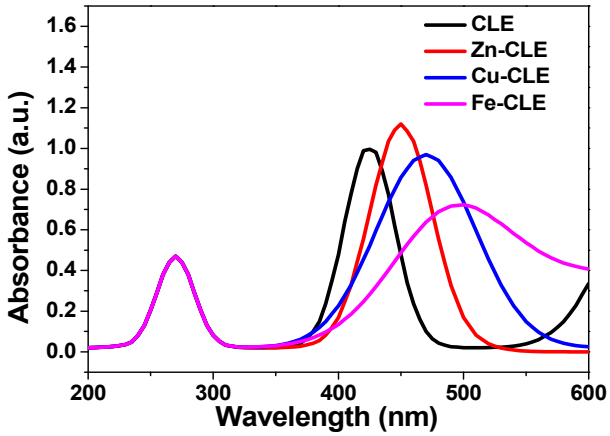

Figure 2. UV-Vis spectra of CLE and its metal complexes.

The CLE showed its highest absorption around 425 nm, which is consistent with expectations for curcumin-type molecules and represents the $\pi \rightarrow \pi^*$ transition of curcumin chromophores [28]. The band was relatively sharp, which implies that CLE will absorb well in the blue region of the solar spectrum. In a DSSC, this absorption helps produce photocurrent from blue photons. But the band dropped quickly after 450–500 nm, so the crude extract alone does not harvest much red light.

When the extract formed a complex with zinc (Zn–CLE), the main band moved to a longer wavelength (red shift). The obtained peak was at 455 nm, and the peak height was slightly larger than that of CLE. This implies that Zn-CLE dye collects slightly more photons in the visible range than CLE. Also, Zn–CLE showed a reasonably clean band (not too broad), which suggests good light harvesting and less chance of extra recombination levels from the metal. The Zn core has a closed-shell d^{10} configuration. It often stabilizes the associated ligand and increases molar absorptivity without adding many new loss pathways. For DSSCs, this often implies somewhat higher J_{sc} and similar V_{oc} [29].

The Cu–CLE seems to have the largest broadening and a peak farther to the red (around 470 nm). The band was wider, and the absorbance remained significant up to about 600 nm. A broad band can harvest more photons across a wider spectral window. But copper, a d-block metal with partially filled d-orbitals, can introduce additional electronic states. This may increase non-radiative losses or act as recombination centers in some cases. Thus, Cu–CLE may give higher J_{sc} from broader absorption, but it may also slightly reduce injection efficiency or increase recombination unless the complex binds well and the metal does not introduce deep trap states [29].

The Fe–CLE showed the largest red shift and the broadest tail. The peak intensity was lower than that of the Zn- and Cu-complexes. Iron can give strong ligand-to-metal or metal-centered transitions and sometimes cause lower molar absorptivity in the ligand band. The long tail into the green-red region helps capture more photons at longer wavelengths, but the lower peak and possible quenching by iron-centred states can reduce quantum yield for electron injection [30]. In practice, Fe–CLE might show improved light harvesting at longer wavelengths, but its contribution to usable photocurrent depends on how well injected electrons avoid recombination.

By comparison of the light harvesting of DSSC, broader and red-shifted bands improve the spectral overlap with sunlight. This usually increases J_{sc} if the injected electrons are collected. Both Zn–CLE and Cu–CLE are likely to give better light harvesting than the crude extract because their absorption extends further into the visible. In terms of electron injection, strong binding to TiO_2 and favourable energy alignment would be needed, as red shift alone may not guarantee good injection. Zinc complexes often help stabilize the ligand and preserve injection efficiency. Copper and iron can change the HOMO–LUMO energies more strongly, so injection behaviour can only be checked experimentally. In terms of recombination and V_{oc}, metals with partly filled d-orbitals (Cu, Fe) can introduce mid-gap states and increase recombination at the dye/TiO_2/electrolyte interface. This may lower the V_{oc} or FF. Zinc (d^{10}) is less likely to cause this, so the V_{oc} may stay similar to the crude extract for Zn–CLE. Finally, in terms of PCE correlation, the PCE should roughly follow the absorbance shapes. Peak PCE are expected near the main absorption maxima. The Zn–CLE and Cu–CLE should show broader IPCE response than CLE.

3.3. FTIR Study

The spectrum of CLE (Figure 3) showed a very broad and strong O-H stretch around 3200–3500 cm^{-1}. This could have come from the phenolic O-H groups and from adsorbed water. The strong band near 1650 cm^{-1} may be assigned to the conjugated carbonyl, the enol form (the keto-enol system) of curcuminoids. This is a key band for curcumin. The medium bands near 1500–1600 cm^{-1} come from aromatic C=C vibrations. The region 1000–1300 cm^{-1} shows strong bands for C–O stretching and C–O–C vibrations from phenolic and enolic parts. In the low frequency region (600–800 cm^{-1}), the crude extract has only weak features.

The specra obtained with the complexes were similar to that of CLE in many ways, but with two main changes. The similarities signify that the key phytocompounds and functional groups in CLE were still present in the complexes, whereas the slight variations signify that the complexation reaction caused chemical modification of some functional groups. First, the strong carbonyl/enol band near 1650 cm^{-1} shifted to lower wavenumbers by some tens of cm^{-1}. For instance, the CLE peak moved to 1620–1640 cm^{-1} for Zn–CLE, to 1610–1630 cm^{-1} for Cu–CLE, and to 1600–1620 cm^{-1} for Fe–CLE. This shift to lower wavenumbers can be considered as a sign that the carbonyl oxygen (or the enolate oxygen) has been coordinated to a metal center. Coordination weakens the C=O bond character, and so the stretching frequency reduces [31].

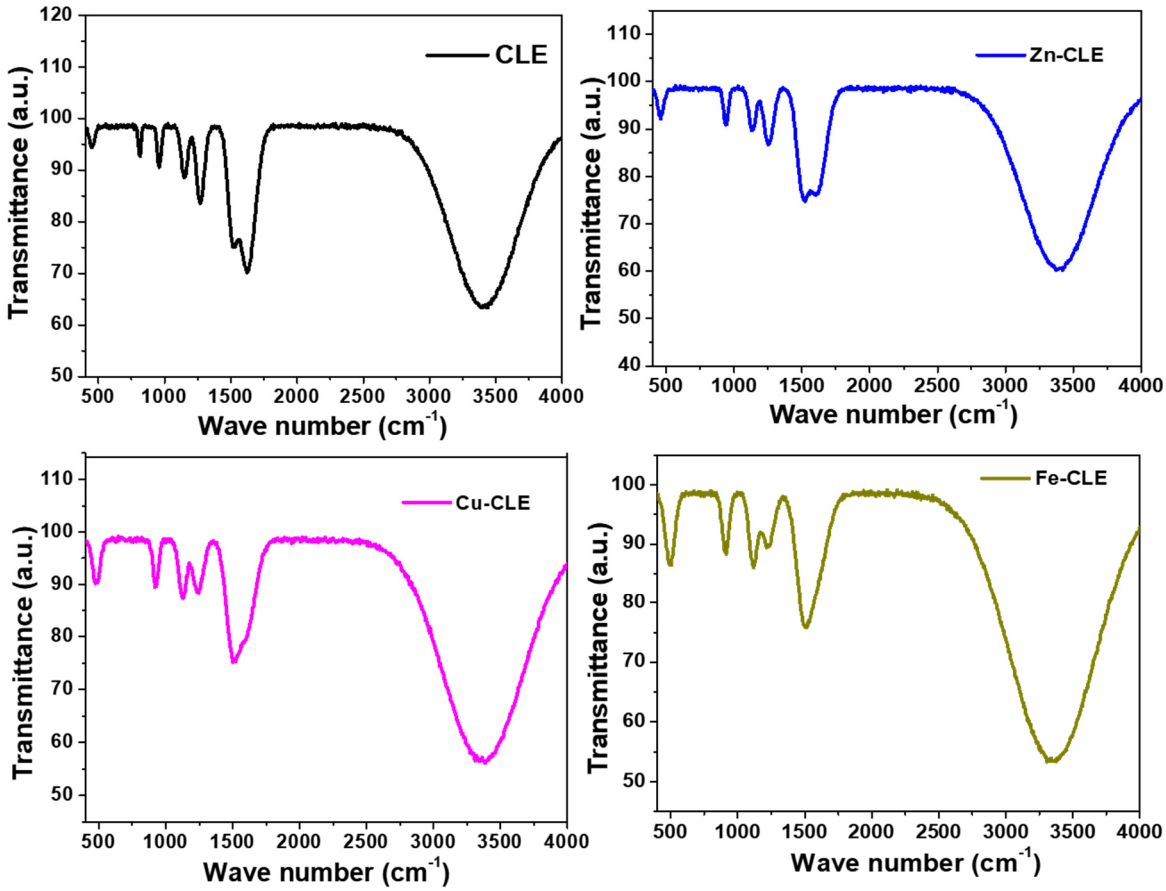

Figure 3. FTIR spectra of CLE and the metal complexes.

Next, stronger bands appeared in the low-frequency region around 500–600 cm^{-1}. These bands may be assigned to metal-oxygen (M–O) vibrations. This band was of small intensity in the spectrum of CLE, but was of relatively larger intensity for the complexes. The exact position and intensity vary with metal; iron showed stronger M–O bands, perhaps due to stronger ligand–metal interactions and higher mass, so Fe–CLE afforded the largest low-frequency band. Other changes were also observed. For instance, the broad O–H band decreased in intensity or narrowed in the complexes, because the phenolic hydrogen may have been involved in coordination or hydrogen-bond changes upon enolate formation. The C–O stretching band (1000–1300 cm^{-1}) shifted a little and changed intensity, perhaps because the metal is bound to oxygen atoms in the ligand. A close observation reveals slight decreases in C–O band intensity for complexes compared to CLE.

In Table 1, the key observations from the FTIR spectra of CLE and the metal complexes are summarized. The significance of these observations can be explained in terms of coordination and DSSC function. The shift in carbonyl peak confirms coordination, that chelation may have occurred through the beta-diketone (keto–enol) moiety of curcumin. This chelation helps stabilize the dye and can reduce fast photodegradation. The appearance of M–O bands near 500–600 cm^{-1} indicates metal binding. The larger M–O intensity for Fe and Cu suggests stronger or more numerous metal–oxygen interactions. Zinc, with d^{10} configuration, still shows M–O features but less strongly than Fe. Changes in O–H and C–O indicate possible deprotonation to form an enolate and stronger anchoring groups. Stronger anchoring can give better dye loading on the TiO_2 surface and more efficient electron injection [32].

On the other hand, for DSSC performance, these spectral changes are encouraging. Coordination through the diketone moiety gives better stability and stronger binding to TiO_2, which usually improves current generation and long-term stability. However, stronger metal–ligand interactions (as likely in Fe- and Cu-complexes) may also change electronic states more strongly, and that can either help or hurt electron transfer depending on energy alignment [33]. Zinc complexes often provide a good balance of coordination for stability and anchoring, with minimal introduction of mid-gap states that cause recombination [34].

Table 1. Summary of FTIR spectral peaks of CLE and its metal complexes following the Sigma-Aldrich Library of FT-IR Spectra.

Vibrational Assignment	CLE (cm^{-1})	Zn-CLE (cm^{-1})	Cu-CLE (cm^{-1})	Fe-CLE (cm^{-1})	Interpretation
O–H stretching (phenolic/enolic, broad)	3220–3460	3205–3440	3198–3435	3190–3425	Broad H-bonded O–H; slight downshift/narrowing on complexation, portraying with H-bond change/partial deprotonation.
C=O/enol (β-diketone) stretching	1646–1660	1620–1640	1610–1630	1600–1620	Clear bathochromic shift on complexation, portrays chelation via carbonyl/enolate O.
Aromatic C=C stretching/conjugation	1500–1520	1502–1510	1498–1508	1495–1506	Minor downshift/intensity changes indicate increased delocalization after coordination.
C–O (enolic/phenolic) stretching and C–O–C	1265–1285	1254–1270	1250–1268	1248–1265	Small redshifts and intensity decrease consistent with O participation in metal binding.
C–H bending/fingerprint	1018–1035	1016–1028	1014–1026	1012–1024	Slight shifts are possibly due to electronic redistribution upon complex formation.
M–O stretching (new/low-freq)	-	515–535	505–525	495–515	New bands in the 500–540 cm^{-1} region portray M–O bond formation; position varies with metal mass and bonding.

3.4. Photovoltaic Performance

The photovoltaic characteristics of the DSSCs sensitized with the CLE and its transition metal complexes were evaluated under standard AM 1.5 G illumination (100 mW cm^{-2}), and the obtained experimental parameters are summarized in Table 2.

Table 2. Some photovoltaic parameters of DSSCs sensitized with *Curcuma longa* extract and its metal complexes.

Sensitizer Material	V_{oc} (mV)	J_{sc} ($mAcm^{-2}$)	FF	η (%)
CLE	360	2.80	0.56	0.57
Zn-CLE	430	4.50	0.62	1.20
Cu-CLE	410	4.10	0.58	0.97
Fe-CLE	390	3.20	0.55	0.69

From the results, it can be inferred that metal complexation considerably enhanced the light-harvesting and charge-transfer properties of the CLE. Among the tested sensitizers, the Zn–CLE complex afforded the highest power conversion efficiency (1.20%), followed by Cu–CLE (0.97%), Fe–CLE (0.69%), and the unmodified extract (0.57%). These results confirm that the introduction of transition metal centers into the curcuminoid structure modifies the electronic configuration of the dye in such a way that it enhances its photovoltaic response.

The superior performance observed for the Zn–CLE device may be attributed to several interrelated factors. Firstly, the result of UV-Vis measurements (Figure 2) had shown that Zn–CLE exhibits a moderate bathochromic shift and an increase in absorption intensity compared to CLE. This red shift may have extended the absorption window further into the visible region, thereby enabling the dye to capture a broader range of solar photons and thus produce a higher J_{sc}. Secondly, the Zn^{2+} ion, having a closed-shell d^{10} configuration, may have acted as a spectator center that stabilizes the ligand without introducing partially filled orbitals that could promote charge recombination. As a result, the electron lifetime within the TiO_2 conduction band got prolonged, leading to a higher V_{oc} and FF compared to other complexes. Moreover, strong chelation between Zn^{2+} and the β-diketone moiety of curcumin may have enhanced anchoring to the TiO_2 surface, thereby improving electron injection efficiency and dye stability under illumination [35]. This synergy could have contributed to making the Zn-CLE device to achieve the highest magnitude of η (%) among the studied sensitizers.

A significant improvement in photovoltaic performance was also observed with Cu–CLE complex device relative to the CLE device. The redshift and broad absorption obtained in the spectrum of Cu–CLE account for its enhanced photon-harvesting capability and higher J_{sc}. However, its V_{oc} and FF were slightly lower than those of Zn-CLE. This can be explained by the partially filled d^9 configuration of Cu^{2+}, which may introduce low-lying electronic states that could facilitate back-electron transfer at the TiO_2/electrolyte interface [36]. Although Cu–CLE exhibited extended absorption and reasonable current generation, partial recombination through these states may have reduced its V_{oc}, resulting in a slightly lower conversion efficiency.

For the Fe–CLE complex, the key observations that were initially pronounced include red shift and broad tailing in the visible region (up to 600 nm), which is consistent with its ligand-to-metal charge transfer (LMCT) character. Theoretically, this broad absorption should favour photon harvesting at longer wavelengths [36]. However, Fe^{3+} has a d^5 configuration, therefore, strong ligand field interactions may introduce deep trap states that compete with efficient electron injection. As a result, Fe–CLE produced moderate J_{sc} and relatively low V_{oc} values, resulting in an overall efficiency of 0.69%. The performance of Fe–CLE signifies that while Fe^{3+} effectively enhanced spectral coverage, its redox activity may have compromised charge separation and stability [37].

In contrast, the crude CLE exhibited the weakest photovoltaic response, with the value of $\eta = 0.57\%$. This relatively low efficiency can be attributed to its narrow absorption range, poor surface binding to TiO_2, and susceptibility to photodegradation. It is also possible that there was limited electron injection from the excited curcuminoid molecules into the TiO_2 conduction band, resulting in lower values of J_{sc} and V_{oc}. Furthermore, owing to the absence of a coordinating metal center, the β-diketone moiety may have become prone to tautomeric instability and self-quenching reactions, which diminished both its stability and charge-transfer efficiency [38].

The overall trend in photovoltaic parameters (Zn–CLE > Cu–CLE > Fe–CLE > CLE) demonstrates that the electronic configuration and coordination geometry of the metal center played critical roles on the DSSC performance. Closed-shell metal ions such as Zn^{2+} stabilize the dye and preserve charge-transfer pathways, while partially filled d-orbitals (Cu^{2+}, Fe^{3+}) can introduce recombination channels that reduce V_{oc} and η despite extended absorption. This is consistent with earlier reports on metal–curcumin and metal–flavonoid complexes, where Zn^{2+} coordination yielded the most balanced performance profile, with a combination of enhanced light absorption, efficient charge injection, and minimized recombination losses [39,40].

3.5. J-V Plots

The J–V curves of the tested devices are shown in Figure 4. All devices exhibited half-depressed semicircular profiles rather than the typical rectangular or sigmoidal shapes observed in optimized DSSCs. Such behaviour suggests significant internal resistance, sluggish charge transport, and interfacial recombination at the dye/TiO_2/electrolyte junctions. Among the tested devices, the Zn–CLE-based cell afforded the highest photocurrent and a less-depressed arc, indicating a comparatively better charge injection and collection [41]. In contrast, Cu–CLE and Fe–CLE displayed more flattened arcs with reduced current densities, and this is consistent with increased recombination and resistive losses, while the CLE-sensitized device produced the lowest response, confirming weak light harvesting and inefficient electron transfer [42].

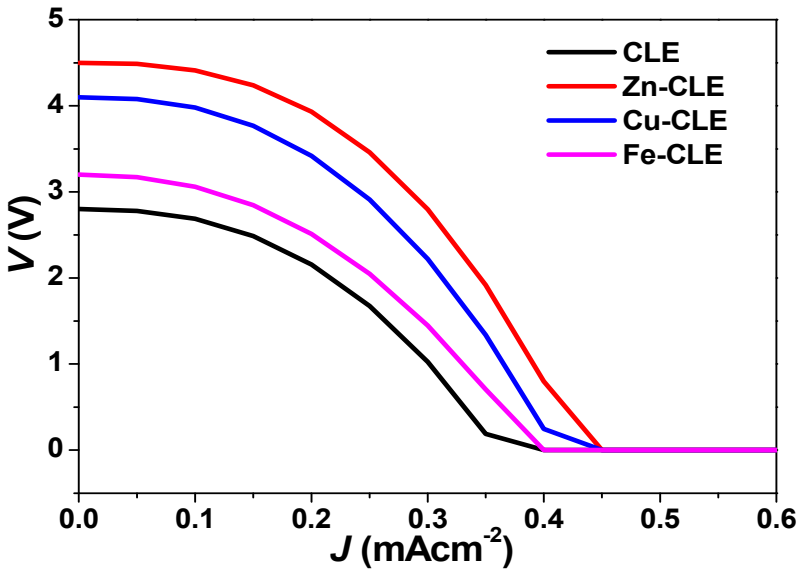

Figure 4. J–V plots for DSSCs sensitized using CLE, Zn–CLE, Cu–CLE and Fe–CLE.

Similar arcs or half-depressed semicircular J–V shapes have been reported for other plant-pigment sensitizers. For instance, anthocyanin-based DSSCs from hibiscus and mulberry extracts exhibited such curved traces, and were attributed to poor dye anchoring and charge recombination through surface trap states [3]. Also, betalain-sensitized cells from

beetroot showed comparable arc-shaped J–V curves, which were linked to internal resistance within the porous TiO_2 network [4]. Similarly, annatto pigments, rich in bixin and norbixin, also produced half-semicircular profiles unless co- when sensitized or chemically modified [22]. Among the complexes, the curve for Zn-CLE is visibly the least depressed, and this may reflect a moderate improvement in electronic coupling and stability, though the overall curvature confirms that the devices still behave within the characteristic performance regime of natural pigment-based DSSCs.

3.6. Photoelectrochemical Properties

The photoelectrochemical parameters of the DSSCs provide further insight into the influence of metal complexation on photon harvesting and charge-transfer processes. The results obtained for the key parameters evaluated are displayed in Table 3.

Table 3. Some photoelectrochemical parameters of DSSCs sensitized with *Curcuma longa* extract and its metal complexes.

Sensitizer Material	λ_{max} (nm)	$A_{\lambda_{max}}$	LHE (%)	PCE (%)	EIR
CLE	420	0.80	61.2	24.5	0.60
Zn-CLE	450	1.14	73.5	39.8	0.87
Cu-CLE	470	1.00	69.1	33.2	0.80
Fe-CLE	480	0.90	65.4	28.9	0.70

The results reveal that the properties of all the devices sensitized using the metal complexes were higher than those of the one sensitized using CLE. This implies that metal complexation significantly enhanced the light-harvesting and charge-transfer properties of the CLE. The highest LHE (73.5%) and IPCE (39.8%) were obtained with Zn-CLE, and this indicates that a larger proportion of photons absorbed by the Zn-CLE device was successfully converted into electrons contributing to photocurrent [43,44]. This superior response can be attributed to a strong coordination of Zn^{2+} with the β-diketone moiety of the curcuminoids, which increases electron delocalization, stabilizes the enolate structure, and improves dye-TiO_2 coupling for efficient electron injection [39].

The devices sensitized by Cu–CLE and Fe–CLE complexes exhibited moderately high LHE values (69–65%), and this seems consistent with their broad absorption spectra, but their IPCE responses were lower than that of Zn–CLE. This portrays that while these dyes captured a comparable amount of light, fewer excited electrons were successfully injected into the TiO_2 conduction band. The partially filled d-orbitals of Cu^{2+} and Fe^{3+} likely introduced intermediate electronic states that facilitated recombination, thereby lowering their effective conversion efficiencies. The CLE-based device exhibited the lowest LHE (61.2%) and IPCE (24.5%). This indicates that the unmodified curcuminoids may have absorbed light efficiently but suffered from poor anchoring and unstable excited-state dynamics, which limit charge separation and promote recombination [40].

Comparable PCE magnitudes have been reported for other plant-derived pigments. For instance, anthocyanin-based DSSCs typically afforded PCE peaks of 20–30% with sharp declines beyond 550 nm [3]; betalain dyes (beetroot) yielded 25–35% IPCE with broad visible absorption [4]; while bixin/norbixin pigments (annatto) afforded about 40% under optimized extraction conditions [22]. The Zn–CLE complex, therefore, matches or surpasses many of these natural dyes, confirming that metal coordination effectively boosts the photoelectrochemical response of the Curcuma longa pigments while maintaining their eco-friendly character.

3.7. Computational Approach

The quantum chemical calculations using DFT/B3LYP were performed on the optimised structure of the curcumin molecule (Figure 5a), the major chromophoric constituent of CLE, and the results are displayed in Table 4. In this section, the computed descriptors are treated, their physical significance for DSSC operation is explained and linked quantitatively and qualitatively to the experimental device observations.

Table 4. Quantum chemical descriptors computed for curcumin using DFT/B3LYP.

Parameter	E_{HOMO}	E_{LUMO}	ΔE	IE	EA	χ	η	σ
Value (eV)	−5.616	−1.726	3.890	5.616	1.726	3.671	1.945	0.514

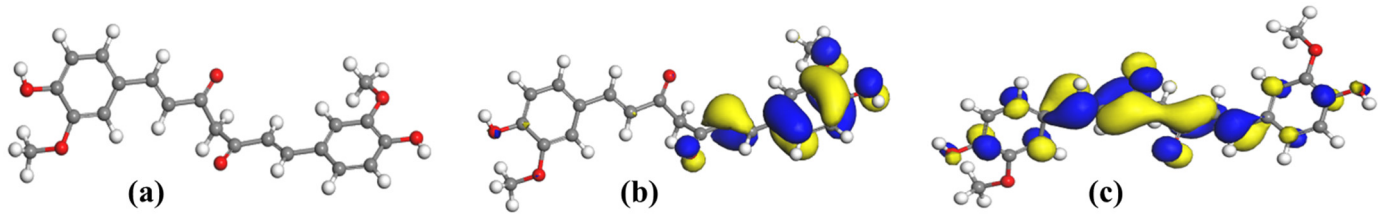

Figure 5. (**a**) Optimized geometry of curcumin; (**b**) HOMO plot of curcumin and (**c**) LUMO plot of curcumin obtained by DFT/B3LYP [C = Grey; O = Red; H = White].

3.7.1. Frontier Orbital Energies and Primary Electronic Structure

The spatial distribution of the HOMO and LUMO orbitals (Figure 5) reveals that the HOMO is primarily localised over the aromatic rings and β-diketone region, while the LUMO extends over the entire π-conjugated backbone. This delocalisation pattern indicates that upon excitation, electron density shifts from the central enolic core toward the peripheral aromatic moieties. This facilitates charge separation and supports efficient electron injection into TiO_2. This orbital arrangement also underlies the characteristic π→π* transition responsible for the main visible absorption band of curcumin, where excitation from the HOMO to the LUMO corresponds to the experimentally observed absorption maximum around 420–430 nm, giving the dye its intense yellow-orange colour. Although the curcumin structure is usually associated with symmetry, a slight asymmetry can be observed in the HOMO and LUMO plots. This arises from the fact that the curcumin molecule was optimized in the gas phase without imposing any symmetry constraints. Under these free conditions, the β-diketone backbone relaxes into a mildly twisted, non-planar geometry, which naturally influences the orbital appearance. This does not indicate an error in the calculation but reflects the optimized structure obtained from the chosen model.

The computed frontier orbital energies yielded E_{HOMO} = −5.616 eV and E_{LUMO} = −1.726 eV which corresponds to a band separation energy (ΔE) of 3.890 eV. The derived global descriptors obtained from the computational study were: IE = 5.616 eV, EA = 1.726 eV, χ = 3.671 eV, chemical potential (μ) = −3.671 eV, η = 1.945 eV, σ = 0.514 eV), and electrophilicity index (ω) = 3.464 eV. The total binding energy was −2396.415 eV (−55,263.7 kcal mol^{-1}), demonstrating a highly stable structure. The relatively large energy gap signifies a strong π→π* transition localised on the conjugated backbone of curcumin. Such a wide gap is consistent with the narrower absorption band observed experimentally for CLE (Figure 2) before metal complexation, indicating limited absorption in the longer-wavelength region. In contrast, dyes with smaller gaps, such as the carotenoids in the Annatto with $\Delta E \approx 1.46$ eV [22], absorb more effectively across the visible spectrum, portraying that curcumin would require further chemical modification to enhance light harvesting.

In DSSCs, the relative positions of the HOMO and LUMO determine electron-injection and dye-regeneration efficiencies. The computed E_{LUMO} (−1.726 eV) lies well above the TiO_2 conduction-band edge, which is about −4.8 eV on the vacuum scale. This indicates that photo-excited curcumin can readily inject electrons into TiO_2. This therefore justifies the non-zero photocurrent densities and measurable PCE values obtained experimentally (Table 3, Figure 5). Conversely, the E_{HOMO} (−5.616 eV) is considerably deeper than the redox potential of the I^-/I_3^- electrolyte, which is about −4.8 eV. This difference represents a sluggish thermodynamic driving force for dye regeneration, and in other words, the possibility of recombination and consequently, limited V_{oc}. From experimental results, the CLE sensitized device exhibited modest V_{oc} (360 mV) and relatively low FF (0.56), and these are consistent with the predicted energetic misalignment between the curcumin HOMO and the electrolyte redox level.

3.7.2. Global Reactivity Descriptors

These set of derived quantum parameters often provide further insight into the behaviour of the dye at the electronic level. The moderate electronegativity (χ = 3.671 eV) and chemical potential (μ = −3.671 eV) indicate that the molecule is capable of accepting electron density but with limited polarisation flexibility [45]. The hardness (η = 1.945 eV) is substantially larger than that of bixin/norbixin (η ≈ 0.73 eV), implying that isolated curcumin is a comparatively "harder", less polarizable system. That also implies that its electron-transfer kinetics are slower, and the crude CLE shows reduced electron-injection efficiency. The inverse relationship is reflected in the global softness (σ = 0.514 eV^{-1}), which corroborates the experimental observation of lower J_{sc} and EIR for CLE relative to its metal complexes. The magnitude of the electrophilicity index (ω = 3.464 eV) implies a moderate tendency to attract electrons, and this is a feature that may favour charge redistribution during excitation but not necessarily enhance long-range charge transport

[45]. In terms of the DSSCdevice, these descriptors collectively explain why curcumin, while being stable and photoactive, yields moderate current densities and efficiencies (η ≈ 0.57%) unless it is structurally modified.

3.7.3. Local Reactivity, Mulliken Charges, and Anchoring Sites

The results of Mulliken charge distribution (Table 5) and Fukui function (f^+ and f^-) analysis (Table 6) reveal strongly negative charge densities on the oxygen atoms of the β-diketone/enolic moiety. The highest f^+ and f^- values occur at O(20), O(21), O(26) and O(27), implying that these atoms can be identified as the principal nucleophilic and electrophilic sites. These positions are therefore the most probable coordination points for metal ions and for anchoring onto TiO_2. This prediction complements the FTIR evidence earlier presented, where shifts in the carbonyl and enolic stretching regions and the emergence of new M–O bands confirmed complex formation. The theoretical localisation of charge at the β-diketone site explains the chelation behaviour inferred from experimental findings and substantiates the inference that the curcumin molecule attaches to TiO_2 through its enolate oxygens rather than through carboxylate groups typical of ruthenium dyes. This alternative binding geometry may affect surface orientation and film packing, thereby influencing recombination resistance and the FF observed in J-V curves (Figure 4).

Table 5. Mulliken atomic charge distribution computed for curcumin using DFT/B3LYP.

Atom	Charge (e)	Atom	Charge (e)	Atom	Charge (e)	Atom	Charge (e)
C(1)	0.275	C(13)	−0.012	O(25)	−0.472	H(37)	0.090
C(2)	0.292	C(14)	0.045	O(26)	−0.466	H(38)	0.063
C(3)	−0.109	C(15)	−0.147	O(27)	−0.465	H(39)	0.064
C(4)	0.050	C(16)	0.312	H(28)	0.095	H(40)	0.250
C(5)	−0.081	C(17)	0.293	H(29)	0.062	H(41)	0.252
C(6)	−0.119	C(18)	−0.120	H(30)	0.060	H(42)	0.070
C(7)	−0.014	C(19)	−0.085	H(31)	0.085	H(43)	0.063
C(8)	−0.129	O(20)	−0.539	H(32)	0.067	H(44)	0.077
C(9)	0.372	O(21)	−0.453	H(33)	0.087	H(45)	0.083
C(10)	−0.258	O(22)	−0.552	H(34)	0.090	H(46)	0.070
C(11)	0.373	O(23)	−0.475	H(35)	0.063	H(47)	0.063
C(12)	−0.139	O(24)	−0.481	H(36)	0.088		

Table 6. Fukui indices computed for curcumin using DFT/B3LYP.

Atom	f^+	f^-	f^0	Atom	f^+	f^-	f^0
C(1)	0.027	0.036	0.031	C(2)	0.019	0.013	0.016
C(3)	0.006	0.020	0.013	C(4)	0.010	−0.011	−0.001
C(5)	0.017	0.015	0.016	C(6)	0.008	0.007	0.007
C(7)	0.009	0.067	0.038	C(8)	0.014	0.008	0.011
C(9)	0.001	0.039	0.020	C(10)	−0.013	−0.025	−0.019
C(11)	0.004	0.033	0.018	C(12)	0.048	0.004	0.026
C(13)	0.002	0.061	0.031	C(14)	0.029	−0.010	0.009
C(15)	0.011	0.019	0.015	C(16)	0.035	0.012	0.023
C(17)	0.044	0.034	0.039	C(18)	0.017	0.006	0.011
C(19)	0.031	0.016	0.023	O(20)	0.043	0.015	0.029
O(21)	0.068	0.029	0.048	O(22)	0.022	0.009	0.015
O(23)	0.035	0.027	0.031	C(24)	−0.017	−0.016	−0.016
C(25)	−0.023	−0.009	−0.016	O(26)	0.019	0.072	0.046
O(27)	0.046	0.064	0.055	H(28)	0.013	0.013	0.013
H(29)	0.026	0.026	0.026	H(30)	0.030	0.034	0.032
H(31)	0.019	0.038	0.028	H(32)	0.016	0.033	0.024
H(33)	0.018	0.048	0.033	H(34)	0.023	0.047	0.035
H(35)	0.029	0.031	0.030	H(36)	0.031	0.034	0.033
H(37)	0.026	0.008	0.017	H(38)	0.049	0.032	0.041
H(39)	0.047	0.025	0.036	H(40)	0.024	0.013	0.019
H(41)	0.015	0.014	0.014	H(42)	0.021	0.019	0.020

H(43)	0.010	0.007	0.009	H(44)	0.016	0.016	0.016
H(45)	0.035	0.023	0.029	H(46)	0.023	0.004	0.014
H(47)	0.019	0.002	0.011				

3.7.4. Observed Discrepancies and Limitations

Some minor quantitative discrepancies between theoretical predictions and experimental data were observed. These arise mainly from the simplified model employed. The DFT calculations were conducted on an isolated curcumin monomer in the gas phase, hence, the solvent, electrolyte, and TiO_2-surface interactions were neglected. Such environmental effects can typically shift orbital energies by several tenths of an electron-volt. Similarly, aggregation of dye molecules in the real film, as indicated by the absorbance features of CLE, is not captured by the isolated molecule approximation. Incorporating explicit metal coordination and surface-adsorbed models, ideally via TD-DFT or periodic slab approaches, would yield a more realistic depiction of interfacial charge transfer processes. The present DFT results describe only the isolated curcumin molecule but do not account for the effects of metal coordination. Although these calculations provide quantitative insight into the electronic nature of the parent curcumin molecule, a complete theoretical understanding of the metal complexes using DFT/TD-DFT modelling of the coordinated systems is recommended for future studies. Future work should therefore include Zn-, Cu- and Fe-curcumin complexes bound to TiO_2 clusters, coupled with electrochemical impedance spectroscopy and transient photovoltage measurements to correlate computed descriptors with kinetic parameters.

3.8. Correlation between Computational and Experimental Findings

The computational and experimental results together provide a coherent mechanistic picture of the performance of *Curcuma longa* extract in DSSCs. The calculated E_{LUMO} indicates efficient electron injection into TiO_2, a prediction borne out by the measurable photocurrents and PCE values of the fabricated devices. Conversely, the deep HOMO explains the limited V_{oc} and FF due to the sluggish regeneration kinetics and increased recombination probability. The large band gap and high hardness are consistent with the comparatively weak visible-light absorption of the unmodified extract, while metal complexation reduces the effective gap and improves light harvesting.

Mulliken and Fukui analyses confirm that the β-diketone/enolate moiety is the active coordination site, which provides a structural rationale for the observed FTIR shifts and the stability of the complexes. The predicted order of performance (Zn > Cu > Fe) arises naturally from differences in the electronic configurations of the coordinating metals and the extent to which each perturbs the ligand orbitals.

Overall, the integration of experimental and theoretical evidence demonstrates that curcumin is an intrinsically stable yet electronically rigid dye whose photovoltaic efficiency depends on chemical modification. The computational descriptors accurately anticipate the observed photovoltaic trends and highlight regeneration kinetics as the primary limitation. This comprehensive correlation between quantum-chemical parameters and device metrics affirms the reliability of the computational approach and provides a firm basis for further design of metal–curcumin and co-sensitised systems with improved efficiencies.

3.9. Comparison with Some Reported Sensitizers

The observed efficiencies were compared to the efficiencies reported for some plant-based dyes in the literature. Natural dyes sensitizers in solar cells typically achieve PCEs below 2%, largely due to limitations in stability, charge transfer and anchoring to semiconductor surfaces [46]. However, a recent review reported that chlorophyll extracted from *Peltophorum pterocarpum* leaves produced a DSSC with a PCE as high as 6.07% [47], which appears to be the highest among many natural dyes studied. Anthocyanin-based dyes have likewise shown significant potential. A recent work using pomegranate-derived anthocyanins achieved a PCE of 0.46% on a TiO_2 photoanode under one-sun illumination [48]. In another study, betanin (a betalain from *Beta vulgaris*) was co-sensitized with chlorophyll, and the combined system delivered 0.601%, performing better than the individual dyes [49]. Furthermore, a ternary mixture of natural dyes from *Beta vulgaris* (betacyanin), *Curcuma longa* (curcuminoids), and *Pandanus amaryllifolius* (chlorophyll) achieved a substantially higher PCE of 3.57%, which demonstrates that there can be synergistic benefits of complementary absorption spectra [50]. Also, anthocyanin-extracted dyes from fruit sources have also shown reasonable performance: for instance, a DSSC sensitized with anthocyanin from mulberry extract attained 0.548% efficiency in earlier reports [51].

The metal complexes, especially Zn–CLE, with a PCE of 1.20%, represent a significant improvement relative to many unmodified plant-dye systems (e.g., anthocyanin or curcumin-only dyes), though it does not reach the very highest reported PCEs such as those observed for chlorophyll-based systems. The performance enhancement afforded by metal complexation in our system underscores the utility of coordination chemistry. Thus, by incorporating transition metal centers into the curcuminoid structure, we appear to modulate the electronic configuration in a way that enhances both light harvesting and charge-transfer. This strategy may therefore offer a promising route to elevate the efficiencies of eco-friendly, bio-derived sensitizers in DSSCs, narrowing the performance gap between natural dyes and synthetic counterparts.

4. Conclusions

This study demonstrates the potential of Zn^{2+}, Cu^{2+} and Fe^{3+} metal complexes of *Curcuma longa* extract as effective sensitizers for DSSCs. Metal complexation significantly enhanced the light-harvesting efficiency and photovoltaic performance of the dye, though a controlled photostability experiment will be required in future studies to verify improvement in photochemical stability quantitatively. Among the complexes, Zn–CLE exhibited the highest power conversion efficiency, owing to its favourable electronic structure and reduced recombination losses, which improve charge transfer. Computational studies further confirm that metal ions enhance electron delocalization, lower the energy gap, and facilitate efficient electron injection into TiO_2. The Zn-CLE complex strikes an optimal balance between light absorption, electron injection, and minimal recombination, making it the most effective sensitizer. This study demonstrates the potential of metal complexation as a strategy to overcome key challenges in using natural plant pigments as DSSC sensitizers, including poor stability and narrow absorption spectra. It also paves the way for developing sustainable, cost-effective alternatives to conventional sensitizers. Future research should focus on a deeper understanding of the chemical composition, structure, mechanism of formation and detailed spectroscopic properties of these complexes.

Statement of the Use of Generative AI and AI-Assisted Technologies in the Writing Process

During the preparation of this manuscript, the author(s) used ChatGPT 5.0 Plus in order to improve language, grammar and structure. After using this tool/service, the author(s) reviewed and edited the content as needed and take(s) full responsibility for the content of the published article.

Acknowledgements

The support of Tertiary Education Trust Fund (TETFund) through TETFund Centre of Excellence in Computational Intelligence Research, is appreciated.

Author Contributions

Conceptualization, E.I.; Methodology, E.I., R.U. and I.O.; Software, E.I. and I.O.; Validation, E.I., R.U., I.O. and U.I.; Formal Analysis, E.I., B.S., R.U., I.O. and S.U.; Investigation, E.I., I.O. and R.U.; Resources, E.I., C.E., B.S., M.A., S.U., R.U., I.O., U.I. and L.O.; Data Curation, E.I., I.O. and R.U.; Writing-Original Draft Preparation, E.I., I.O., R.U., S.U., C.E, B.S. and L.O.; Writing—Review & Editing, E.I., C.E., B.S., M.A., S.U., R.U., I.O., U.I. and L.O.; Visualization, E.I., U.I. and L.O.; Supervision, E.I.; Project Administration, E.I. and U.I.; Funding Acquisition, E.I. and U.I., please turn to the CRediT taxonomy for the term explanation.

Ethics Statement

Not applicable.

Informed Consent Statement

Not applicable.

Data Availability Statement

All data generated or analyzed during this study are included in this published article.

Funding

This research received no external funding.

Declaration of Competing Interest

The authors declare that they have no known competing financial interests or personal relationships that could have appeared to influence the work reported in this paper.

References

1. Carella A, Borbone F, Centore R. Research progress on photosensitizers for DSSC. *Front. Chem.* **2018**, *6*, 481. doi:10.3389/fchem.2018.00481.
2. Abdellah IM. Molecular engineering and electrolyte optimization strategies for enhanced performance of Ru (ii) polypyridyl-sensitized DSSCs. *RSC Adv.* **2025**, *15*, 9763–9786. doi:10.1039/D5RA01470K.
3. Pramananda V, Fityay TAH, Misran E. Anthocyanin as natural dye in DSSC fabrication: A review. *Mater. Sci. Eng.* **2021**, *1122*, 012104. doi:10.1088/1757-899X/1122/1/012104.
4. Güzel E, Arslan BS, Durmaz V, Cesur M, Tutar ÖF, Sarı T, et al. Photovoltaic performance and photostability of anthocyanins, isoquinoline alkaloids and betalains as natural sensitizers for DSSCs. *Sol. Energy* **2018**, *173*, 34–41. doi:10.1016/j.solener.2018.07.048.
5. Teja AS, Srivastava A, Satrughna JAK, Tiwari MK, Kanwade A, Lee H, et al. Synergistic co-sensitization of environment-friendly chlorophyll and anthocyanin-based natural dye-sensitized solar cells: An effective approach towards enhanced efficiency and stability. *Sol. Energy* **2023**, *261*, 112–124. doi:10.1016/j.solener.2023.06.004.
6. Sabagh S, Izadyar M, Arkan F. Photovoltaic properties of the flavonoid-based photosensitizers: Molecular-scale perspective on the natural dye solar cells. *Int. J. Quantum Chem.* **2020**, *120*, e26171. doi:10.1002/qua.26171.
7. Alegbe EO, Uthman TO. A review of history, properties, classification, applications and challenges of natural and synthetic dyes. *Heliyon* **2024**, *10*, e33646. doi:10.1016/j.heliyon.2024.e33646.
8. Kim HJ, Kim DJ, Karthick SN, Hemalatha KV, Raj CJ. Curcumin dye extracted from *Curcuma longa* L. used as sensitizers for efficient dye-sensitized solar cells. *Int. J. Electrochem. Sci.* **2013**, *8*, 8320–8328. doi:10.1016/S1452-3981(23)12891-4.
9. Sofyan N, Situmorang FW, Ridhova A, Yuwono AH, Udhiarto A. Visible light absorption and photosensitizing characteristics of natural yellow 3 extracted from *Curcuma longa* L. for dye-sensitized solar cell. *Earth Environ. Sci.* **2018**, *105*, 012073. doi:10.1088/1755-1315/105/1/012073.
10. Anoua R, Lifi H, Touhtouh S, El Jouad M, Hajjaji A, Bakasse M, et al. Optical and morphological properties of *Curcuma longa* dye for dye-sensitized solar cells. *Environ. Sci. Pollut. Res.* **2021**, *28*, 57860–57871. doi:10.1007/s11356-021-14551-9.
11. Yuliasari F, Nuraini U, Aeni AR, Hidayat R. Fabrication of dye-sensitized solar cells with natural dye pigments derived from mustard green (*Brassica juncea* L.) and turmeric (*Curcuma longa* L.). *J. Phys. Conf. Ser.* **2024**, *2866*, 012013. doi:10.1088/1742-6596/2866/1/012013.
12. Ogunsolu OO, Braun AJ, Robb AJ, Salpage SR, Zhou Y, Hanson K. Influence of dye-coordinated metal ions on electron transfer dynamics at dye–semiconductor interfaces. *ACS Appl. Energy Mater.* **2018**, *2*, 29–36. doi:10.1021/acsaem.8b01559.
13. Tripathy L, Sarangi AK. Coordination dynamics: The role of azodye metal ions in enhancing polymeric behaviour. *J. Indian Chem. Soc.* **2025**, *102*, 101734. doi:10.1016/j.jics.2025.101734.
14. Saleh AM, Abd El-Wahab Z, Ali OA, Faheim AA, Salman AA. Performance of new metal complexes for anionic and cationic dyes photodegradation: Construction, spectroscopic studies, optical properties, and DFT calculations. *Res. Chem. Intermed.* **2023**, *49*, 3287–3326. doi:10.1007/s11164-023-05049-9.
15. Bhagat KK, Cheke RS, Gavali VD, Kharkar PS, Arote ND. A brief review on metal–curcumin complexes: Synthesis approaches and their pharmaceutical applications. *Discov. Chem.* **2025**, *2*, 119. doi:10.1007/s44371-025-00174-3.
16. Nawaz S, Manjunatha KB, Supriya S, Ranganatha S, Ranjan P, Chakraborty T, et al. Zinc-curcumin complexes: Design, synthesis, geometry optimization, and optical nonlinearity applications. *Opt. Mater.* **2023**, *143*, 114164. doi:10.1016/j.optmat.2023.114164.
17. Barik A, Mishra B, Shen L, Mohan H, Kadam RM, Dutta S, et al. Priyadarsini KI. Evaluation of a new copper (II)–curcumin complex as superoxide dismutase mimic and its free radical reactions. *Free Radic. Biol. Med.* **2005**, *39*, 811–822. doi:10.1016/j.freeradbiomed.2005.05.005.
18. Özbolat G, Yegani AA, Tuli A. Synthesis, characterization and electrochemistry studies of iron (III) complex with curcumin ligand. *Clin. Exp. Pharmacol. Physiol.* **2018**, *45*, 1221–1226. doi:10.1111/1440-1681.12964.
19. Takagi K, Magaino S, Saito H, Aoki T, Aoki D. Measurements and evaluation of dye-sensitized solar cell performance. *J. Photochem. Photobiol. C Photochem. Rev.* **2013**, *14*, 1–12. doi:10.1016/j.jphotochemrev.2012.08.003.
20. Kutlu N. Investigation of electrical values of low-efficiency dye-sensitized solar cells (DSSCs). *Energy* **2020**, *199*, 117222. doi:10.1016/j.energy.2020.117222.

21. Khan MJ, Ahirwar A, Sirotiya V, Rai A, Varjani S, Vinayak V. (2023). Nanoengineering TiO_2 for evaluating performance in dye sensitized solar cells with natural dyes. *RSC Adv.* **2023**, *13*, 22630–22638. doi:10.1039/d3ra02927a.
22. Ituen E, Okon I, Usoro R, Umana S, Udoisoh M, Inyang U. Harnessing nature's colours: Experimental and computational insights into bixa orellana pigments for next-generation dye-sensitized solar cells. *Green Chem. Technol.* **2025**, *2*, 10010. doi:10.70322/gct.2025.10010.
23. Park J, Do S, Lee M, Ha S, Lee KG. Preparation of turmeric powder with various extraction and drying methods. *Chem. Biol. Technol. Agric.* **2022**, *9*, 39. doi:10.1186/s40538-022-00307-1.
24. Beshah TD, el Gazar S, Farag MA. Curcuminoids: A multi-faceted review of green extraction methods and solubilization approaches to maximize their food and pharmaceutical applications. *Adv. Sample Prep.* **2025**, *13*, 100159. doi:10.1016/j.sampre.2025.100159.
25. Manasa P, Kamble AD, Chilakamarthi U. Various extraction techniques of curcumin—A comprehensive review. *ACS Omega* **2023**, *8*, 34868–34878. doi:10.1021/acsomega.3c04205.
26. Alim MA, Repon MR, Islam T, Mishfa KF, Jalil MA, Aljabri MD, et al. Mapping the progress in natural dye-sensitized solar cells: Materials, parameters and durability. *ChemistrySelect* **2022**, *7*, e202201557. doi:10.1002/slct.202201557.
27. Sen S, Mascoli V, Liguori N, Croce R, Visscher L. Understanding the relation between structural and spectral properties of light-harvesting complex II. *J. Phys. Chem. A* **2021**, *125*, 4313–4322. doi:10.1021/acs.jpca.1c01467.
28. Kushwaha P, Shukla B, Dwivedi J, Saxena S. Validated high-performance thin-layer chromatographic analysis of curcumin in the methanolic fraction of *Curcuma longa* L. rhizomes. *Future J. Pharm. Sci.* **2021**, *7*, 178. doi:10.1186/s43094-021-00330-3.
29. Božić-Weber B, Constable EC, Hostettler N, Housecroft CE, Schmitt R, Schönhofer E. The d^{10} route to dye-sensitized solar cells: Step-wise assembly of zinc(II) photosensitizers on TiO_2 surfaces. *Chem. Commun.* **2012**, *48*, 5727–5729. doi:10.1039/c2cc31729j.
30. Mauri L, Colombo A, Dragonetti C, Roberto D. A fascinating trip into iron and copper dyes for DSSCs. *Inorganics* **2022**, *10*, 137. doi:10.3390/inorganics10090137.
31. Baiz CR, McRobbie PL, Anna JM, Geva E, Kubarych KJ. Two-dimensional infrared spectroscopy of metal carbonyls. *Acc. Chem. Res.* **2009**, *42*, 1395–1404. doi:10.1021/ar9000263.
32. Zhang L, Cole JM. Anchoring groups for dye-sensitized solar cells. *ACS Appl. Mater. Interfaces* **2015**, *7*, 3427–3455. doi:10.1021/am507334m.
33. Muñoz-García AB, Benesperi I, Boschloo G, Concepcion JJ, Delcamp JH, Gibson EA, et al. Dye-sensitized solar cells strike back. *Chem. Soc. Rev.* **2021**, *50*, 12450–12550. doi:10.1039/D0CS01336F.
34. Lu J, Liu S, Wang M. Push-pull zinc porphyrins as light-harvesters for efficient dye-sensitized solar cells. *Front. Chem.* **2018**, *6*, 541. doi:10.3389/fchem.2018.00541.
35. Vallejo W, Lerma M, Díaz-Uribe C. Dye sensitized solar cells: Meta-analysis of effect sensitizer-type on photovoltaic efficiency. *Heliyon* **2025**, *11*, e41092. doi:10.1016/j.heliyon.2024.e41092.
36. Lakhdar R, Freyria FS, Mousdis GA, Bonelli B, Elghniji K. Salicylic acid-modified Sm-TiO_2 for photoluminescence and photocatalysis under real sunlight: synergistic effects between ligand-to-metal charge transfer (LMCT) and Sm^{3+} dopant. *J. Phys. Chem. C* **2024**, *128*, 13445–13457. doi:10.1021/acs.jpcc.4c03459.
37. Sharma K, Sharma V, Sharma SS. Dye-sensitized solar cells: Fundamentals and current status. *Nanoscale Res. Lett.* **2018**, *13*, 381. doi:10.1186/s11671-018-2760-6.
38. Mari M, Carrozza D, Malavasi G, Venturi E, Avino G, Capponi PC, et al. Curcumin-based β-diketo ligands for Ga^{3+}: Thermodynamic investigation of potential metal-based drugs. *Pharmaceuticals* **2022**, *15*, 854. doi:10.3390/ph15070854.
39. Walencik PK, Choińska R, Gołębiewska E, Kalinowska M. Metal–flavonoid interactions—From simple complexes to advanced systems. *Molecules* **2024**, *29*, 2573. doi:10.3390/molecules29112573.
40. Septiani S, Rahmalia W, Usman T. Performance test of Zn-astaxanthin complex-sensitized solar cell: Effect of light intensity on open-circuit voltage and short-circuit current values. *Turk. J. Chem.* **2024**, *48*, 210–217. doi:10.55730/1300-0527.3653.
41. Tripathi B, Yadav P, Kumar M. Charge transfer and recombination kinetics in dye-sensitized solar cell using static and dynamic electrical characterization techniques. *Sol. Energy* **2014**, *108*, 107–116. doi:10.1016/j.solener.2014.06.037.
42. Han L, Koide N, Chiba Y, Islam A, Mitate T. Modeling of an equivalent circuit for dye-sensitized solar cells: Improvement of efficiency of dye-sensitized solar cells by reducing internal resistance. *Comptes Rendus Chim.* **2006**, *9*, 645–651. doi:10.1016/j.crci.2005.02.046.
43. Arjmand F, Ranjbar ZR. Effect of dye complex structure on performance in DSSCs; An experimental and theoretical study. *Heliyon* **2022**, *8*, e11692. doi:10.1016/j.heliyon.2022.e11692.
44. Mahadik SA, Pathan HM, Salunke-Gawali S. An overview of metal complexes, metal-free and natural photosensitizers in dye-sensitized solar cells. *Energy Environ.* **2024**, *24*, 1078. doi:10.30919/esee1078.
45. Ituen E, Okon I, Shaibu S, Donald A, Samuel S, Inyang U. Evaluation of Avocado Peels Dye as Sensitizer in Dye-Sensitized Solar Cells by Experiment and Computational Intelligence. *Adv. Energy Convers. Mater.* **2024**, *5*, 21–30. doi:10.37256/aecm.5120243743.

46. Kusumawati Y, Hutama AS, Wellia DV, Subagyo R. Natural resources for dye-sensitized solar cells. *Heliyon* **2021**, *7*, e08436. doi:10.1016/j.heliyon.2021.e08436.
47. Triyanto A, Ali NA, Salleh H, Setiawan J, Yatim NI. Development of natural dye photosensitizers for dye-sensitized solar cells: A review. *Environ. Sci. Pollut. Res.* **2024**, *31*, 31679–31690. doi:10.1007/s11356-024-33360-4.
48. Leela Devi V, De D, Kuchhal P, Pachauri RK. Photovoltaic performance of TiO_2 and ZnO nanostructures in anthocyanin dye-sensitized solar cells. *Clean Energy* **2024**, *8*, 144–156. doi:10.1093/ce/zkae059.
49. Sreeja S, Pesala B. Co-sensitization aided efficiency enhancement in betanin–chlorophyll solar cell. *Mater. Renew. Sustain. Energy* **2018**, *7*, 25–37. doi:10.1007/s40243-018-0132-x.
50. Kusumawati N, Setiarso P, Muslim S, Zakiyah N, Rahmawati K, Fachrirakarsie FF. Optimizing Dye-Sensitized Solar Cell (DSSC) Performance through Synergistic Natural Dye Combinations from *Beta vulgaris* L., *Curcuma longa* L., and *Pandanus amaryllifolius*. *Indones. J. Chem.* **2024**, *24*, 1675–1687. doi:10.22146/ijc.93830.
51. Chang H, Lo YJ. Pomegranate leaves and mulberry fruit as natural sensitizers for dye-sensitized solar cells. *Sol. Energy* **2010**, *84*, 1833–1837. doi:10.1016/j.solener.2010.07.009.